A Nanoindentation Study of The Plastic Deformation and Fracture Mechanisms in Single-Crystalline $CaFe_2As_2$

Keara G. Frawley[1], Ian Bakst[2], John T. Sypek[1], Sriram Vijayan[1], Christopher R. Weinberger[2], Paul C. Canfield[3], Mark Aindow[1], Seok-Woo Lee[1,*]

1. *Department of Materials Science and Engineering & Institute of Materials Science, University of Connecticut, 97 North Eagleville Road, Unit 3136, Storrs CT 06269-3136, USA*
2. *Department of Mechanical Engineering, Colorado State University, Fort Collins CO 80523,USA*
3. *Ames Laboratory & Department of Physics and Astronomy, Iowa State University, Ames IA 50011, USA*

Corresponding Author:

Seok-Woo Lee

- **Address)** Department of Materials Science and Engineering & Institute of Materials Science, 97 North Eagleville Road, Unit 3136 Storrs, CT 06269-3136, USA
- **Email)** seok-woo.lee@uconn.edu
- **Telephone)** +1 860-486-8028

Abstract:

In the present work, the plastic deformation and fracture mechanisms in single-crystalline $CaFe_2As_2$ were studied using nanoindentation and Density Functional Theory simulations. $CaFe_2As_2$ single crystals were grown in a Sn-flux, resulting in homogeneous and nearly defect-free crystals. Nanoindentation along the [001] direction produces strain bursts, radial cracking, and lateral cracking. Ideal cleavage simulations along the [001] and [100] directions using density functional theory calculations revealed that cleavage along the [001] direction requires a much lower stress than cleavage along the [100] direction. This strong anisotropy of cleavage strength implies that $CaFe_2As_2$ has an atomic-scale layered structure, which typically exhibits lateral cracking during nanoindentation. This special layered structure results from weak atomic bonding between the (001) Ca and Fe_2As_2 layers.

Keywords: intermetallic compound, nanoindentation, plasticity, and fracture

INTRODUCTION

$ThCr_2Si_2$-type intermetallic compounds have been widely investigated due to their unique electronic and magnetic properties [1]. The FeAs-based pnictides are particularly attractive due to their high temperature superconductivity and tunable properties through the application of pressure [2-7]. Among several FeAs-based pnictides, $CaFe_2As_2$ has been the most widely studied, due to the strong pressure sensitivity of its material properties and lattice structure.

We recently discovered superelasticity and cryogenic shape memory effects in this material since the collapsed tetragonal phase transition can be reversed once the applied force is released [8]. Micropillar compression along the c-axis showed a nearly 13% elastic limit and a high yield strength of 3 GPa. $CaFe_2As_2$ also exhibits ultra-high elastic energy absorption and release capability per unit volume, 10~1000 times higher than those of high strength alloys and ceramics. Furthermore, because of the large hysteresis observed during loading and unloading below 50K, there should also be a linear shape memory effect. $CaFe_2As_2$ is also expected to have superior fatigue resistance due to the fact that the geometry of the phase transformation does not lead to the accumulation of any residual stresses or dislocations. Therefore, $CaFe_2As_2$ is attractive not only as an electronic/magnetic material but also as a structural material.

Due to its strong potential as a structural material, it is important to characterize the deformation and fracture behavior of this compound in more detail. Nanoindentation on intermetallic compounds, which are typically relatively brittle, usually induce plastic deformation and fracture at the same time. Thus, nanoindentation is an excellent technique for investigating the mechanical behavior of intermetallic compounds. In this

study, we used nanoindentation to study the plastic deformation and fracture behavior of $CaFe_2As_2$ and found three unique mechanical behaviors: strain bursts, radial cracking, and lateral cracking. Strain bursts and radial cracking can be understood by conventional indentation plasticity and cracking mechanisms. We also performed Density Functional Theory (DFT) calculations to elucidate the microscopic origins of lateral cracking. DFT simulations revealed that ideal cleavage along the (001) planes requires a much lower stress than for cleavage along the {100} planes, keeping in mind that in the tetragonal structure the (001) planes and {100} planes are different. This strong anisotropy of cleavage strength implies that $CaFe_2As_2$ has an atomic-scale layered structure, which usually shows lateral cracking during nanoindentation. Our results help to provide a more in-depth understanding of plasticity and fracture processes in $CaFe_2As_2$, and will be useful in the development of mechanically robust devices using this compound.

EXPERIMENTAL DETAILS

The solution growth method used to produce single crystals of $CaFe_2As_2$ is described in detail elsewhere [8, 9]. The crystals obtained typically have sizes of up to 5x5x1 mm^3 (Fig. 1(a)). The microstructure and composition of the $CaFe_2As_2$ crystals were analyzed using transmission electron microscopy (TEM) (Tecnai T-12, FEI, OR, USA operated at 120 kV) and energy dispersive x-ray spectrometry (EDXS) in the scanning electron microscope (SEM) (Teneo LoVac, FEI, OR, USA operated at 30 kV), respectively. Nanoindentation was performed at room temperature using an iNano^{TM} system (Nanomechanics, Inc., TN, USA). A standard Berkovich tip nanoindentation technique was performed along the [001] direction with an indentation strain rate of 0.2 s^-

[1] and indentation depths of 60, 100, 150, and 600 nm. A Helios Nanolab^{TM} 460F1 (FEI, OR, USA) dual-beam SEM and focused ion beam (FIB) system was used to investigate the indent morphologies and to prepare FIB-cut lamellae for TEM investigation

COMPUTATIONAL DETAILS

In order to simulate the nature of fracture in $CaFe_2As_2$, we utilized density functional theory (DFT) to compute the cleavage energy and the ideal cleavage strength along particular crystallographic directions in both the orthorhombic (O) and collapsed tetragonal (CT) structures of $CaFe_2As_2$. Two different planes were chosen, the (001) plane, between both Ca-As layers and Fe-As layers, and the (100) plane, which was chosen for comparison with the (001) and is different in the orthorhombic and tetragonal crystals. To compute the cleavage energy of the (001) plane, four unit cells along the [001] direction were utilized for a total length of 45.9 Å. For the (100) planes, eight unit cells along the [100] direction were used with a total length of 31.9 Å. The supercells were then relaxed with fully periodic boundary conditions, and antiferromagnetic stripe ordering was used for the O structure. Then, sequentially, a vacuum gap was introduced between select atomic planes to simulate the cleavage process, and the total energy and stress (derivative of the energy with respect to displacement) were determined, a process outlined in [10]. The simulations were carried out using the Vienna Ab initio simulation package (VASP) [11-14], a plane wave DFT code, using the the Perdew–Burke–Ernzerhof (PBE) exchange-correlation functions [15, 16], the projector augmented wave (PAW) pseudo-potentials [17, 18], 450 eV plane wave cutoff and Monkhost-Pack integration scheme of 9x9x1 integration points for the O unit cell.

RESULTS AND DISCUSSION

EDXS at four different locations shows that the area average composition (Ca:Fe:As=19.97:40.13:39.90 at.%) is very close to the ideal 1:2:2 stoichiometry. A bright-field (BF) scanning transmission electron microscope (STEM) image obtained in the FIB/SEM, and higher magnification BF TEM images, show that our sample is initially free of dislocations and inhomogeneities (Fig. 1(b)). This is in stark contrast to the layer structure exhibited by $BaFe_2As_2$ [19], which is another $ThCr_2Si_2$-type intermetallic compound. There is some Sn residue on the surface of the $CaFe_2As_2$ crystals, because they are grown in a Sn-flux. Care was taken to obtain indentations while avoiding contact between the indenter and the Sn residue.

A standard Berkovich nanoindentation technique was performed on the (001) plane with three different indentation depths, 60, 100, and 150 nm (Fig. 2(a)-(c)). Load-displacement curves show that the first three strain bursts occur at similar load and displacement values (Fig. 2(a)-(c)). SEM images of the sample surface show two distinct features; residual indents and radial cracks (Fig 2(d)-(f)). Strain bursts should be related to plastic deformation that forms the residual indents since radial cracking usually does not produce strain bursts in load-displacement curves. Our previous work using micropillar compression along the [001] direction and DFT simulations suggests that strain is accommodated by plastic deformation on the $\frac{1}{2}\langle 31\bar{1}\rangle\{103\}$ slip system [20]. Thus, the residual indent would be formed primarily by dislocation plasticity in this slip system. TEM and EDXS analyses show that our sample is dislocation-free and chemically homogeneous prior to deformation. Thus, the first strain burst in the load-

displacement curves should be associated with dislocation nucleation, rather than the activation of pre-existing dislocation sources. In the case of the activation of pre-existing dislocation sources, the onset displacements and the sizes of the strain bursts usually vary within a wide range, because the activation of the dislocation source depends strongly on its statistical distribution. However, dislocation nucleation usually shows a more consistent behavior. Similarly, micropillar compression on dislocation-free body-centered-cubic molybdenum alloy pillars shows a consistent onset displacement and stress for dislocation nucleation [21]. Once dislocations are introduced into these molybdenum pillars, however, these two values vary significantly from pillar to pillar because source activation is sensitive to a given dislocation structure [22]. The onset displacement and strain bust size were plotted as a function of the onset load (Fig. 2(g) and 2(g)). These plots clearly show consistent onset load for the initial strain burst amongst the samples. So, the chemically homogeneous and dislocation-free microstructure of $CaFe_2As_2$ results in the consistent load and displacement conditions of the first strain burst.

The second and third strain bursts also occur at relatively similar indentation conditions, but the onset displacement and the size of strain burst are more scattered than those of the first strain burst (Fig. 2(g) and 2(h)). The second and third strain bursts are not necessarily associated with dislocation nucleation. They could also be related to the operation of dislocation sources, which the first dislocation nucleation event could produce. It is extremely difficult to confirm experimentally whether the second and third pop-in events occur due to the nucleation of new dislocations or due to the operation of

potentially newly created dislocation source. So, at this point, we are not able to provide a clear picture of dislocation process for the second and third events.

All strain bursts in load-displacement curves exhibit the slightly upward slope. This upward slope would be related to the slow propagation of the resultant pop-in instabitily, i.e. a result of the low mobility of the dislocations. We measured the displacement rate during the pop-in events, which is about 50~100 nm/sec. This value is much lower than that of metals, which are typically over 1000 nm/sec at similar load levels. This result implies that the pop-in instability in $CaFe_2As_2$ propagates relatively slowly, and this could be related to the low mobility of dislocations. This upward slope of the strain bursts is typically observed in nanoindentation of ceramics, ionic crystals, and intermetallic compounds, which have the relatively low mobility of dislocation [23-25].

The observation of radial cracking (the white arrows in Fig. 2(d)-(f)) is likely a result of the difficulty of activating sufficient slip systems to carry plastic deformation outside the confinement created by the indenter, resulting in fracture. Once the size of the radial crack becomes sufficiently large, the load distribution spreads resulting in strain bursts with wider distributions (Fig. 3(a)). We also found surface pop-out (the red broken arrows in Fig. 2(f)) for indentation depths larger than 100 nm. For the indentation depth of 600 nm (Fig. 3(a)), a large area of the surface completely moves along the unloading direction (Fig. 3(b)). This is certainly different from pile-up, which is usually caused by the plastic flow of material. By using FIB, we carefully examined a cross-section of the region underneath the indent, and found that lateral cracks were present. Such lateral cracks are typically observed in indentation of thin films on substrates or of multi-layered materials [26] (Fig. 3(c)). MAX phases ($M_{n+1}AX_n$, (MAX) where n = 1 to 3), which have

a layered-like atomic structure, also exhibit lateral cracking under indentation. Based on the TEM analysis, our material does not have a macroscopic layered-like structure, and thus we conclude that $CaFe_2As_2$ behaves similarly to MAX phases [27]. Lateral cracks always form during unloading as a result of atomic buckling driven by plastic deformation on the (001) plane that creates residual stresses during loading. During unloading, the geometric constraint of the indenter is removed slowly allowing the structure to buckle and fracture along the (001) planes [28]. To understand how bonding in $CaFe_2As_2$ is responsible for the fracture process we utilized DFT to examine ideal fracture.

Figure 4 shows the ideal cleavage simulations from DFT for both the O and CT phases. In the experiments at room temperature, the crystal structure is tetragonal, which is crystallographically similar to the O phase with both being larger than the CT phase along the c-axis by roughly 10%. The use of the O phase as a substitute for the tetragonal phase can be found in [8, 20]. The cleavage simulations demonstrate that it is much easier to cleave the (001) Ca-As planes (Figure 4(c)) as compared to the (001) Fe-As planes (Figure 4(d)) and the (100) planes. This is a direct result of the cage structure created by the bonding between iron and arsenic, a key feature of the $ThCr_2Si_2$ structure. The results in Figure 4(c) and (d) demonstrate that the cleavage energy and cleavage stress are 2-3 times lower for the Ca-As (001) plane. This, in conjunction with the equally favorable slip on this plane through Generalized Stacking Fault (GSF) calculations [20], clearly demonstrates that this material behaves in a micaceous-like manner with easy slip and cleavage on the same plane, resulting in very anisotropic properties. We note that this is a result of the weak bonding between the Ca and Fe_2As_2 layers, creating an atomically

layered material. Our previous micropillar studies [20] also support these DFT results. During uni-axial compression, [1 1 3] micropillars exhibit extensive easy slip in the $\langle 100 \rangle (001)$ system, implying that the atomic bonding between the (001) planes is weak. Thus, the atomic-scale layered structure of $CaFe_2As_2$ is similar to MAX phases, which also exhibit lateral cracking during nanoindentation [27].

Finally, we can summarize the deformation and fracture behavior for loading and unloading conditions (Fig. 5). During loading, plastic deformation occurs in two primary slip systems, the $\frac{1}{2}\langle 31\bar{1} \rangle \{103\}$ and $\langle 100 \rangle (001)$. Dislocation nucleation and propagation in the $\frac{1}{2}\langle 31\bar{1} \rangle \{103\}$ slip system forms the residual indents because the Burgers vector of these dislocations have a vertical component, a necessary feature for indentation formation under loading in this orientation. Dislocation nucleation and propagation of the $\langle 100 \rangle (001)$ slip system is not able to contribute to the residual indents, but can produce plastic deformation along lateral directions and are likely created to maintain material compatibility. Flow on this slip system ultimately results in residual stresses which contribute to the driving force for material buckling and lateral cracking. When the indenter tip is retracted, buckling of (001) layers occurs to relax the compressive residual stresses created by these dislocations, resulting lateral cracking. Based on DFT simulation, the lateral cracking occurs between (001) Ca and As layers due to their weak bonding. Finally, radial cracks also form at the sharp edge of the Berkovich tip due to stress concentrations and the limited number of, as pointed out above, the low mobility of easy slip systems in the compound. The lack of or low mobility of dislocation sources are also common in ceramics, which frequently exhibit radial cracking during indentation.

CONCLUSION

We conducted a standard Berkovich nanoindentation study to help develop a better understanding of the plastic deformation and fracture behavior of $CaFe_2As_2$. Three major deformation mechanisms were found: strain bursts, radial cracking, and lateral cracking. The strain bursts are related to the nucleation of $\frac{1}{2}\langle 31\bar{1}\rangle\{103\}$ dislocations under the indenter, which is a consequence of the lack of dislocation sources. Radial cracking is also present away from the indent, a result of the reduced constraint. Lateral cracking results from the atomically layered structure of $CaFe_2As_2$. DFT simulations reveal that ideal cleavage occurs on the (001) plane much more easily than the (100) plane, which confirms that $CaFe_2As_2$ possesses an atomic-scale layered structure. This special layered structure results from weak atomic bonding between the (001) Ca and Fe_2As_2 layers.

ACKNOWLEDGEMENTS

K.G. Frawley, J. T. Sypek, and S.-W Lee acknowledge support from the UConn Start-up Funding and the Early Career Faculty Grant from NASA's Space Technology Research Grants Program. SEM, FIB and TEM experiments were performed using the facilities in the UConn/Thermo Fisher Scientific Center for Advanced Microscopy and Materials Analysis (CAMMA). Work by P.C. Canfield was supported by the U.S. Department of Energy, Office of Basic Energy Science, Division of Materials Sciences and Engineering. Their research was performed at the Ames Laboratory. Ames Laboratory is operated for the U.S. Department of Energy by Iowa State University under Contract No. DE-AC02-07CH11358. This work utilized the RMACC Summit supercomputer, which is supported

by the National Science Foundation (awards ACI-1532235 and ACI-1532236), the University of Colorado Boulder and Colorado State University.

References

[1] R. Hoffmann, C. Zheng, *J. Phys. Chem.*, 89, 4175 (1985).

[2] P. C. Canfield, S. L. Bud'ko, N. Ni, A. Kreyssig, A. I. Goldman, R. J. McQueeney, M. S. Torikachvili, D. N. Argyriou, G. Luke, W. Yu, *Physica C*, 469, 404 (2009).

[3] N. Ni, S. Nandi, A. Kreyssig, A. I. Goldman, E. D. Mun, S. L. Bud'ko, P. C. Canfield, *Phys. Rev. B,* 78, 014523 (2008).

[4] T. Park, E. Park, H. Lee, T. Klimczuk, E. D. Bauer, F. Ronning, J. D. Thompson, *J. Phys.: Condens. Matter*, 20, 322204 (2008).

[5] J. Zhao, D. T. Adroja, D. -X. Yao, R. Bewley, S. Li, X. F. Wang, G. Wu, X. H. Chen, J. Hu, P. Dai, *Nat. Phys.*, 5, 555 (2009).

[6] K. Kudo, K. Iba, M. Takasuga, Y. Kitahama, J. Matsumura, M. Danura, Y. Nogami, Minoru Nohara, *Sci. Rep.*, 3, 1478 (2013).

[7] A. I. Goldman, A. Kreyssig, K. Prokeš, D. K. Pratt, D. N. Argyriou, J. W. Lynn, S. Nandi, S. A. J. Kimber, Y. Chen, Y. B. Lee, G. Samolyuk, J. B. Leão, S. J. Poulton, S. L. Bud'ko, N. Ni, P. C. Canfield, B. N. Harmon, R. J. McQueeney, *Phys. Rev. B*, 79, 024513 (2009).

[8] J. T. Sypek, H. Yu, K. J. Dusoe, G. Drachuck, H. Petal, A. M. Giroux, A. I. Goldman, A. Kreyssig, P. C. Canfield, S. L. Bud'ko, C. R. Weinberger, S. -W. Lee, *Nat. Commun.*, 8, 1083 (2017).

[9] P. C. Canfield, Z. Fisk, *Philos. Mag. B*, 65, 1117 (1992).

[10] H. Yu, G. B. Thompson, C. R. Weinberger, *Extreme Mech. Lett.*, 17, 1 (2017).

[11] G. Kresse, J. Hafner, *Phys. Rev. B*, 47, 558 (1993).

[12] G. Kresse, J. Hafner, *Phys. Rev. B*, 49, 14251 (1994).

[13] G. Kresse, J. Furthmüller, *Comput. Mat. Sci.*, 6, 15 (1996).

[14] G. Kresse, J. Furthmüller, *Phys. Rev. B*, 54, 11169 (1996).

[15] J. P. Perdew, K. Burke, M. Ernzerhof, *Phys. Rev. Lett.*, 77, 3865 (1996).

[16] J. P. Perdew, K. Burke, M. Ernzerhof, *Phys. Rev. Lett.*, 78, 1396 (1997).

[17] P. E. Blochl, *Phys. Rev. B*, 50, 17953 (1994).

[18] G. Kresse, D. Joubert, *Phys. Rev. B*, 59, 1758 (1999).

[19] G. B. de Souza, F. C. Serbena, A. R. Jurelo, S. A. da Silva, L. B. L. G. Pinheiro, F. T. Dias, A. Mikowski, S. L. Bud'ko, A. Thaler, P. C. Canfield, *J. Mater. Res.*, 30, 1413 (2016).

[20] J. T. Sypek, C. R. Weinberger, S. Vijayan, M. Aindow, S. L. Bud'ko, P. C. Canfield, S. -W. Lee, *Scr. Mater.*, 141, 10 (2017).

[21] H. Bei, S. Shim, E. P. George, M. K. Miller, E. G. Herbert, G. M. Pharr, *Scr. Mater.*, 57, 397 (2007).

[22] H. Bei, S. Shim, G. M. Pharr, E. P. George, *Acta Mater.*, 56, 4762 (2008).

[23] U. Ramamurty, J.-I. Jang, *Cryst. Eng. Comm.*, 16, 12-23 (2014).

[24] S. Bhagavat, I. Kao, *Mater. Sci. Eng. A*, 393, 327-331 (2005).

[25] M. A. Lodes, A. Hartmaier, M. Göken, K. Durst, *Acta Mater.*, 59, 4264-4273 (2011).

[26] R. D. Jamison, Y. L. Shen, *Surf. Coat. Technol.*,, 303, 3 (2016).

[27] T. A. Prikhna, S. N. Dub, A. V. Starostina, M. V. Karpets, T. Cabiosh, P. Chartier, *J. Superhard Mater.*, 34, 102 (2012).

[28] J.W. Hutchinson, Z. Suo, Adv. Appl. Mech., 29, 62 (1992).

FIGURE 1. (a) Optical macrograph of a $CaFe_2As_2$ single crystal (b) BF STEM (left) and TEM (right) images showing a homogeneous defect-free internal structure. The inset [100] zone axis selected area diffraction pattern confirms the orientation of the crystal.

FIGURE 2. Load-displacement curves (a-c) and SEM images (d-f) for indentations with depths of: (a,d) 60 nm, (b,e) 100 nm, (c,f) 150 nm. In (c)-(e), the white arrows indicate the radial cracks, and the red broken arrows indicate the surface pop-out. The values of the onset displacement and the size of the first three strain bursts are shown in (g) and (h) as a function of the onset load, respectively. The onset displacement and load are the displacement and load values at which a strain burst starts. The size of strain burst is the displacement change between its onset and offset.

FIGURE 3. Data from an indentation with a depth of 600 nm: (a) Load-displacement curve; (b,c) SEM images of: (b) the indent before FIB milling, and (c) a FIB-cut cross-section showing sub-surface lateral cracks.

FIGURE 4. DFT simulations of the cohesive traction-separation: (a) a schematic diagram of traction-separation; energy vs. displacement curve for separation, (b) the actual supercells of $CaFe_2As_2$ used illustrating the different directions in the tetragonal structure and the blue box outlines the standard tetragonal unit cell, (c) (0 0 1) Ca-As and Fe-As planes along the [0 0 1] direction, and (d) (1 0 0) planes along the [1 0 0] direction. The stress required for separation in each inset is calculated by taking the derivative of the energy per unit area with respect to displacement.

FIGURE 5. Schematics of the indentation deformation and fracture for (a) loading and (b) unloading conditions. (a) During loading, it is possible to nucleate both $\frac{1}{2}\langle 31\bar{1}\rangle\{103\}$

and $\langle 100 \rangle (001)$ dislocation. The former are shown as inclined to the vertical axis while the lateral appear normal to it and cannot contribute to the residual indent but are likely necessary for maintaining material compatibility. Additionally, the formation of radial cracks, due to stress concentrations and the low mobility of dislocations, also form. (b) During unloading, the residual $\langle 100 \rangle (001)$ dislocations likely create residual stresses that, when the applied load is removed, which drives local buckling. Due to the weak bonding between (001) Ca and Fe_2As_2 layers, the material separates forming lateral cracks.

FIGURE 1

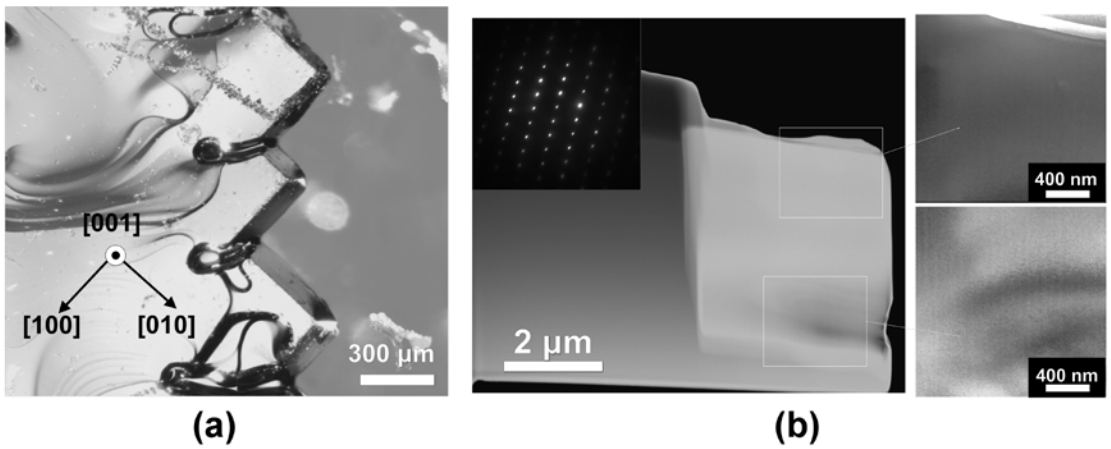

FIGURE 2

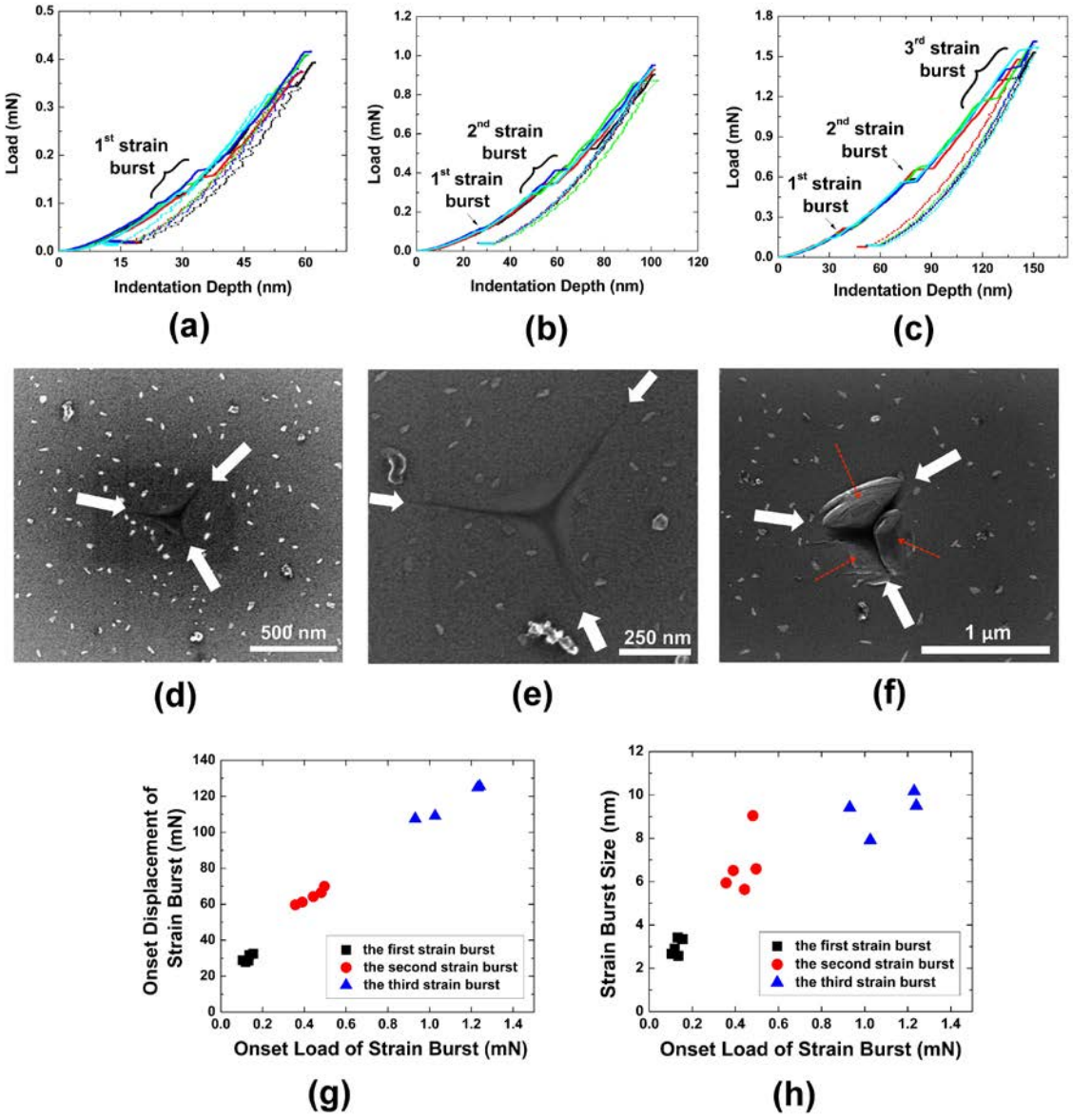
Load (mN)
Indentation Depth (nm)
1st strain burst
2nd strain burst
3rd strain burst
(a)
(b)
(c)
500 nm
250 nm
1 μm
(d)
(e)
(f)
Onset Displacement of Strain Burst (mN)
Onset Load of Strain Burst (mN)
Strain Burst Size (nm)
the first strain burst
the second strain burst
the third strain burst
(g)
(h)

FIGURE 3

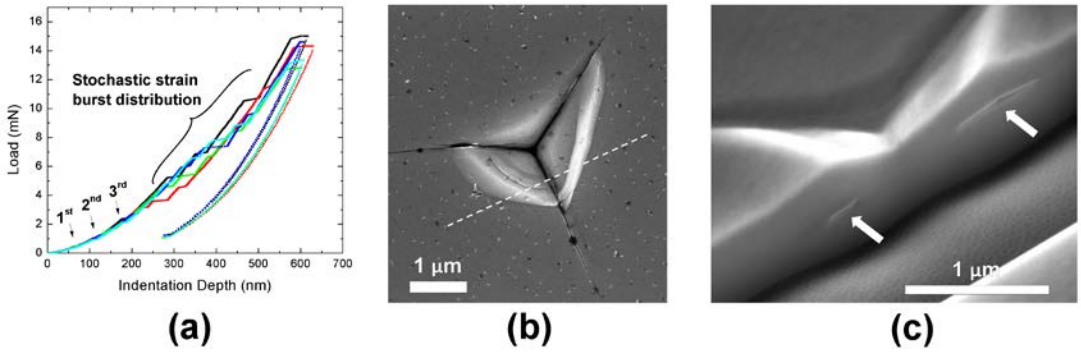
Stochastic strain
burst distribution
1st
2nd
3rd
Load (mN)
Indentation Depth (nm)
0
2
4
6
8
10
12
14
16
0
100
200
300
400
500
600
700
1 µm
1 µm

(a) (b) (c)

FIGURE 4

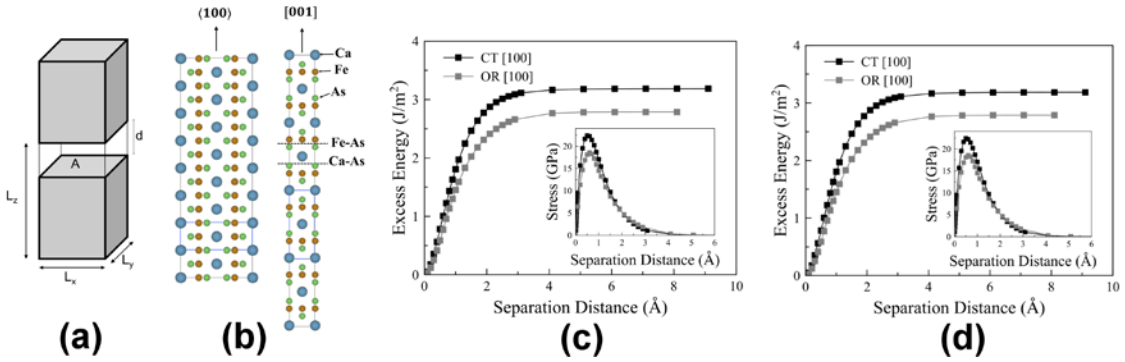
(100)
[001]
Ca
Fe
As
Fe-As
Ca-As
d
A
L_z
L_x
L_y
(a)
(b)
CT [100]
OR [100]
Excess Energy (J/m^2)
Stress (GPa)
Separation Distance (Å)
(c)
CT [100]
OR [100]
Excess Energy (J/m^2)
Stress (GPa)
Separation Distance (Å)
(d)

FIGURE 5

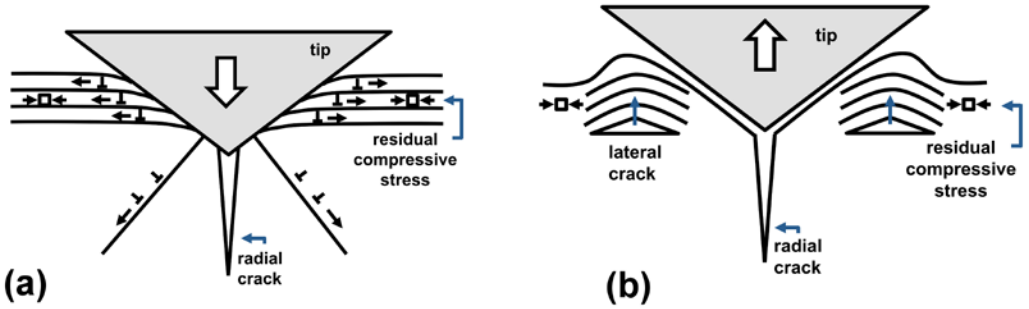
tip
residual
compressive
stress
radial
crack
(a)
tip
lateral
crack
residual
compressive
stress
radial
crack
(b)